ACSNANO

www.acsnano.org

ARTICLE

In Situ Thermal Conductivity Measurement of Single-Crystal Zeolitic Imidazolate Framework-8 by Raman-Resistance Temperature Detectors Method

Jun Huang, Aoran Fan, Xiaoxiao Xia, Song Li,* and Xing Zhang*

Cite This: *ACS Nano* 2020, 14, 14100−14107

Read Online

ACCESS | Metrics & More | Article Recommendations | Supporting Information

ABSTRACT: The thermal conductivity measurement of metal−organic frameworks (MOFs), which plays an important role in thermal management of MOF-based gas separation, storage, and thermal energy conversion (*e.g.*, adsorption heat pumps), has been a challenging task for decades. However, the direct thermal conductivity measurement of a single-crystal MOF is currently limited by their small crystal sizes, since no sophisticated approach has ever been reported. In this study, the Raman-resistance temperature detectors (Raman-RTDs) method was developed for *in situ* measuring of the thermal conductivity of single-crystal ZIF-8, whose system error resulting from the thermal contact resistance between sample and RTDs can be eliminated. According to the dependence of thermal resistance of MOF crystals on the laser spot location, the thermal conductivities of polycrystalline and single-crystal ZIF-8 were derived to be 0.21 ± 0.03 and 0.64 ± 0.09 W/(m·K), respectively. The proposed *in situ* thermal conductivity measurement method may be further extended to other types of microscale particles.

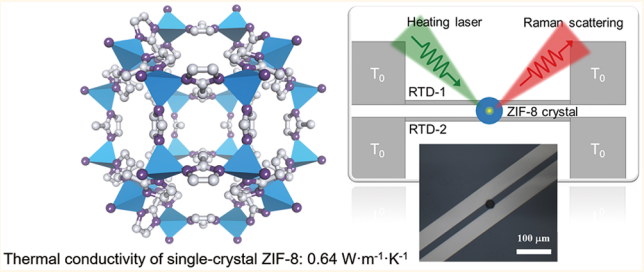

KEYWORDS: *metal−organic framework, thermal conductivity, thermal contact resistance, Raman shift, single crystal*

Metal−organic frameworks (MOFs) consisting of metal clusters and organic linkers have been identified as promising sorbent materials for gas adsorption related applications such as hydrogen storage,[1,2] gas separation,[3,4] adsorption heat pumps,[5,6] and harvesting water from air[7,8] because of their extremely large surface area and high porosity.[9,10] During adsorption/desorption processes, heat is released from or absorbed by MOF adsorbents. Such exothermic or endothermic processes can significantly change the temperature of the adsorption bed and sequentially affect the adsorption rate and capacity.[11] Therefore, thermal management is crucial for rapid and efficient gas adsorption by MOFs. Prior to the thermal management, determining the thermal conductivity of MOFs is crucial for understanding their heat transfer mechanism as well as thermally designing MOF-based gas adsorption/storage systems. However, the thermal conductivity measurement of MOFs is extremely challenging, especially directly measuring the single-crystal MOFs, since no sophisticated approach has ever been reported.

In previous studies, most thermal conductivity measurements of MOFs were implemented on compacted MOF powders, which are usually below 0.22 $W \cdot m^{-1} \cdot K^{-1}$ due to the extensive thermal contact resistance between MOF particles.[12−16] Therefore, several efforts have been made to improve the thermal conductivity of MOFs by adding high-conductivity additives or tuning their heat conduction pathway by uniaxial compression.[17−20] Nevertheless, the different contributions of the interparticle thermal contact resistance and the thermal conductivity of a MOF crystal to the effective thermal conductivity of MOF composites are very difficult to quantify. This is a common issue for not only the compacted powder of MOFs but also other microscale particles.[21−23] Thus, it is of great significance to directly measure the thermal conductivity of a MOF crystal.

Received: August 12, 2020
Accepted: September 2, 2020
Published: September 2, 2020

https://dx.doi.org/10.1021/acsnano.0c06756
ACS Nano 2020, 14, 14100−14107

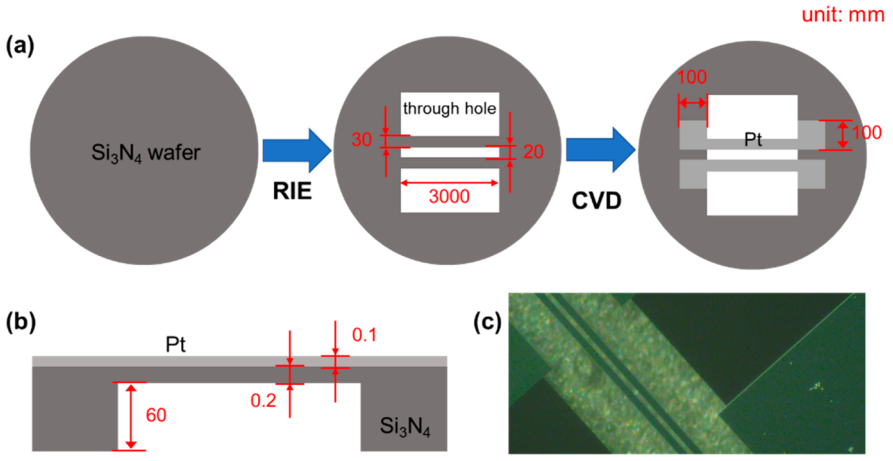

Figure 1. Fabrication of the suspended Pt/Si_3N_4 RTDs. (a) Fabrication process and in-plane size parameters; (b) cross-section structure; (c) optical profiler image of the suspended RTDs.

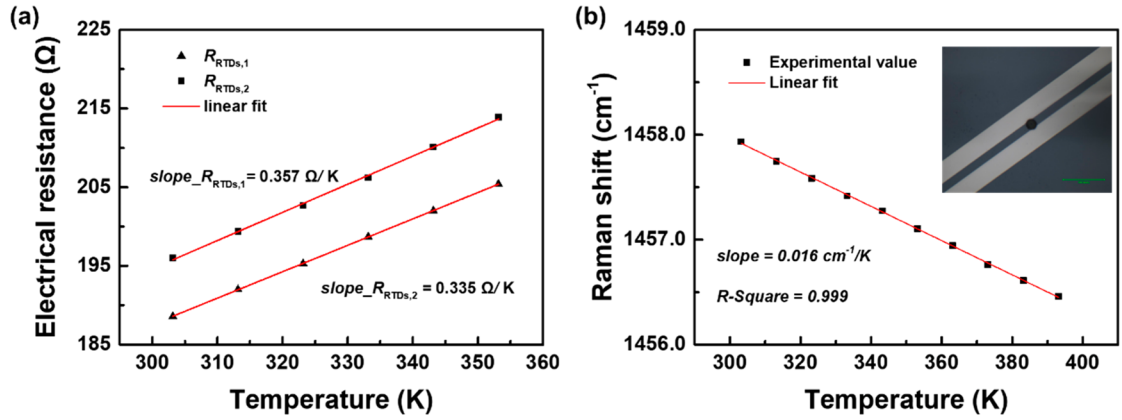

Figure 2. Measurement calibration. (a) Relationship between electrical resistance of RTDs and temperature; (b) dependence of Raman peak shift of ZIF-8 on the temperature. The inset is an optical profiler image of the ZIF-8 crystal in between two Si_3N_4/Pt RTDs.

However, direct measurement of the thermal conductivity of a MOF crystal is limited by the relatively large sample size required for current measurement approaches. Heretofore, only a very few types of MOFs that can be grown to the order of millimeters have been measured by a steady-state method directly.[24,25] Although many thermal conductivity measurement approaches have been proposed for microscale materials, such as the microdevice method,[26,27] T-type method,[28] 3-ω method,[29] and transient thermoreflectance method,[30] all suffer from a system error resulting from the thermal contact resistance between the sample and the temperature sensor. Recently, the dual-wavelength flash Raman spectroscopy method[31,32] that can measure the thermal conductivity of the sample and the thermal contact resistance between sample and substrate simultaneously was proposed. However, these methods mentioned above are only suitable for one- and two-dimensional materials rather than microscale particles due to the difficulties in obtaining the heat flux/temperature distributions on the heterogeneous surface of the sample. The measurement error resulting from thermal contact resistances between sample and the temperature sensors is also a great obstacle in accurately describing the thermal conductivity of microscale particles. Therefore, *in situ* thermal conductivity measurement of microscale single crystals is still a great challenge.

Herein, we developed the Raman-resistance temperature detectors (Raman-RTDs) method for *in situ* measuring the thermal conductivities of MOF crystals and measured the thermal conductivity of the ZIF-8 crystal because of its wide applications in ethanol/water separation[33] and adsorption-driven heat pumps.[34] The thermal conductivity measurement was conducted at a temperature of 303.15 K in a vacuum. The tested crystal was heated by a continuous laser, and the temperature of the heating spot was deduced from its Raman peak shift. The sample was supported by two Si_3N_4/Pt cantilever beams, which acted as resistance temperature detectors to monitor the temperature variation of the contact regions and the heat flux flowing out of the sample. Then, the thermal resistances between laser heating spot and cold contact points were derived by dividing the temperature difference by the heat flux. According to the dependence of the measured thermal resistance on the laser spot location, the thermal conductivity of a ZIF-8 crystal and the thermal contact resistance between the sample and RTDs can be quantified simultaneously, which helps to eliminate the system error caused by thermal contact resistances.

RESULTS AND DISCUSSION

The ZIF-8 crystal was synthesized from zinc nitrate hexahydrate and 2-methylimidazole by the solvothermal method (see Methods and Figures S1−5 in the Supporting

https://dx.doi.org/10.1021/acsnano.0c06756
ACS Nano 2020, 14, 14100−14107

Information (SI) for details) and placed in between the two homemade suspended Si_3N_4/Pt RTDs, which were fabricated by reactive ion etching (RIE) and the chemical vapor deposition (CVD) method, as shown in Figure 1. The electrical resistance of two RTDs was measured respectively as a function of temperature from 303 to 353 K (Figure 2a). The electrical resistance linearly deceases with increasing temperature, which indicates a high measurement accuracy of temperature. The distance of the contact point to the two ends of the RTDs (L_1 and L_2), the temperature coefficient of resistance (a_0), and the thermal conductivity (k_b) of the RTDs are summarized in Table 1 (see Figures S6 and S7 for details of the thermal conductivity measurement of RTDs). Figure 2b shows the temperature dependence of the Raman peak shifts from 303 to 393 K of the ZIF-8 crystal. The slope of the temperature dependence is −0.016 cm^{-1}/K (see detailed Raman spectra of the tested ZIF-8 crystal in Figure S8).

Table 1. Parameters of the Fabricated Pt/Si_3N_4 RTDs

	L_1 (mm)	L_2 (mm)	a_0 (K^{-1})	k_b ($W{\cdot}m^{-1}{\cdot}K^{-1}$)
RTDs-1	1651.5	1330.6	0.00188	362.78
RTDs-2	1651.5	1330.6	0.00175	386.60

The schematic of the Raman-RTDs method is demonstrated in Figure 3. During the measurement, the heat flux flows from the laser spot to the contact regions between the sample and suspended RTDs. Then it is transferred to the four heat sinks linked to the end of RTDs. When the crystal was heated to steady state, the temperature rise of the heating spot (ΔT_h) was deduced from the Raman scattering spectroscopy. Meanwhile, the temperature rise of the contact region (ΔT_c) and the heat flux (Q) could be derived from the average temperature rise of the RTDs (ΔT_{av}) according to eqs 1 and 2.

$$\Delta T_c = 2\Delta T_{av} = 2\frac{\Delta R}{\alpha_0 R_0} \tag{1}$$

$$Q = k_b A \Delta T_c \left(\frac{1}{L_1} + \frac{1}{L_2}\right) \tag{2}$$

where ΔR and R_0 represent the change and initial value of the RTDs' electrical resistance, respectively; α_0 is the temperature coefficient of resistance of the RTDs; A is the cross-section area of RTDs; L_1 and L_2 are lengths of the RTDs on each side of the contact region; and k_b denotes the thermal conductivity of the RTDs. The heat flux flows from the laser spot to contact regions inside the sample. The heat conduction pathways are represented by "heat pathway 1" and "heat pathway 2" as illustrated in Figure 4a. The corresponding thermal resistances between the laser heating spot and the contact region are denoted as R_{L1} and R_{L2}. The two thermal contact resistances between sample and RTDs are represented by R_{c1} and R_{c2}. Therefore, the measured thermal resistance of the sample can be written as

$$R_i = R_{Li} + R_{ci} = \frac{\Delta T_h - \Delta T_{c,i}}{Q_i} \tag{3}$$

where the subscript i represents the two heat conduction pathways (i = 1, 2). The measured thermal resistance (R_i) consists of the effective thermal resistance of the tested particle and the thermal contact resistance between the sample and the RTDs, which commonly exists in contact methods and may cause a system error during the thermal conductivity measurement. Our Raman-RTDs method aims to eliminate this system error with the help of the dependence of thermal resistances of the sample on the laser spot location. As the laser spot moves toward one of the contact points (*i.e.*, "contact 1" in Figure 4a), the effective length of "heat pathway 1" becomes shorter and "heat pathway 2" becomes longer. Then, R_{L1} decreased and R_{L2} increased. Meanwhile, the thermal contact resistances between sample and RTDs remained constant. As a result, the change of R_{L1} and R_{L2} can be represented by the measured results of R_1 and R_2. Furthermore, by considering the difference between two measured thermal resistances, $\Delta R = R_1 - R_2$, the measurement error can be further reduced. So, the thermal conductivity of the sample can be derived accurately from the dependence of ΔR on the laser spot location (x) without the influence of thermal contact resistances between sample and RTDs.

The three-dimensional heat conduction problem of a sphere particle with a diameter of 21.6 μm corresponding to the tested

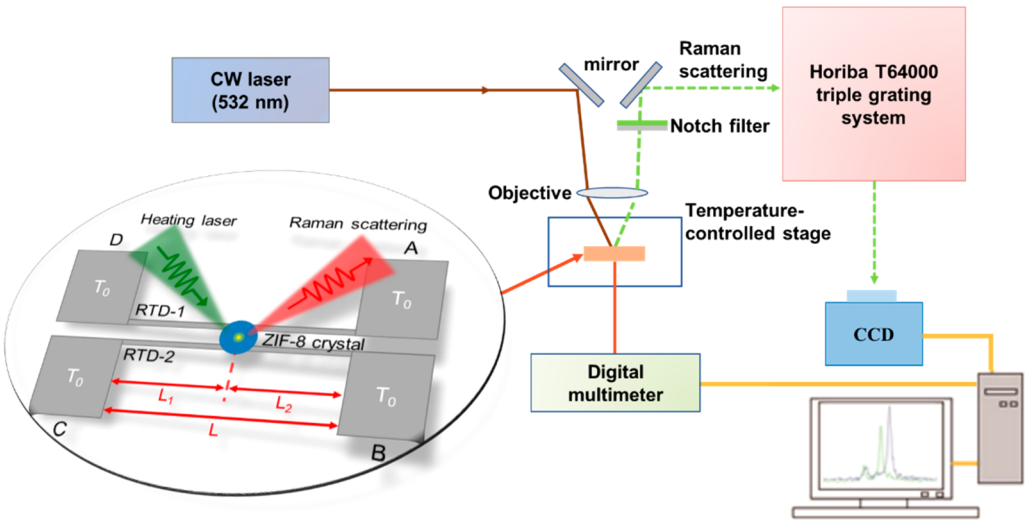

Figure 3. Schematic of the Raman-RTDs method for measuring the thermal conductivity of the ZIF-8 single crystal.

https://dx.doi.org/10.1021/acsnano.0c06756
ACS Nano 2020, 14, 14100−14107

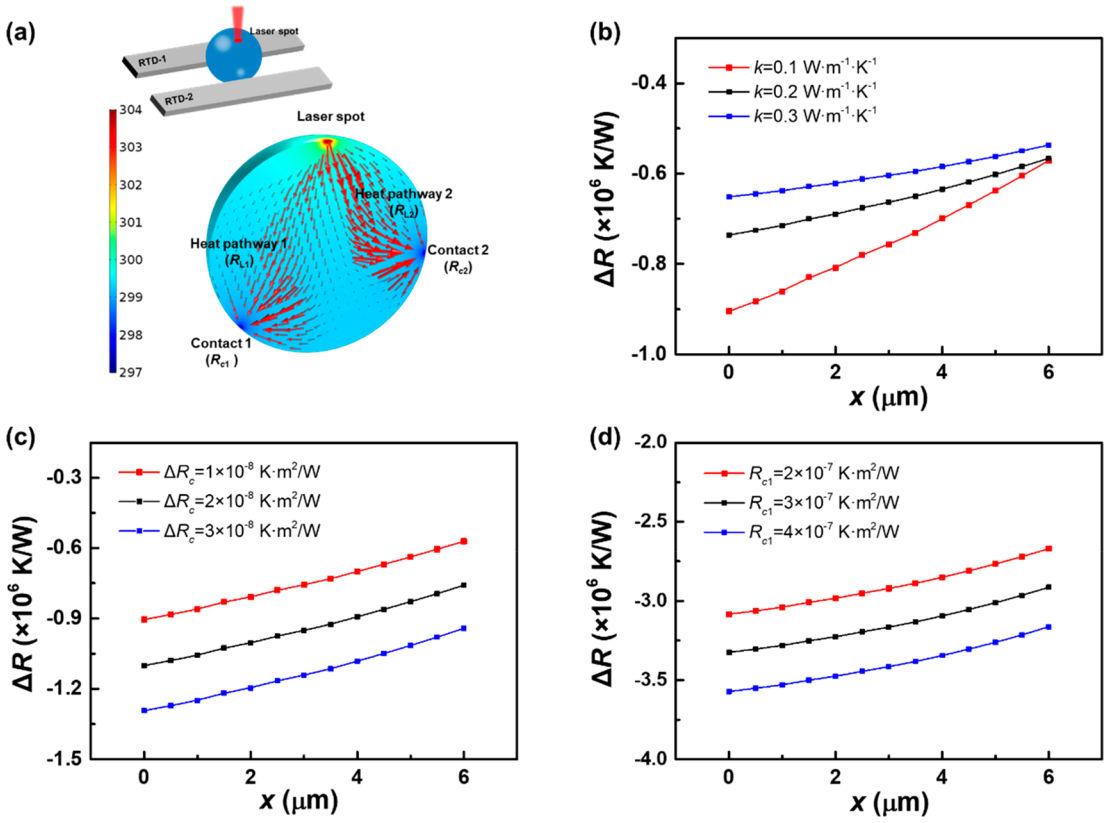

Figure 4. Different effects of thermal conductivity of the tested sample and thermal contact resistances between sample and RTDs on the thermal resistance difference *versus* laser spot location (ΔR–x) curve. (a) Physical model of the three-dimensional steady-state heat conduction problem; (b) thermal contact resistances (R_{c1} and R_{c2}) are fixed and thermal conductivity (k) changes; (c) k and R_{c1} are fixed and the difference between two thermal contact resistances ($\Delta R_c = R_{c1} - R_{c2}$) varies; (d) R_{c1} and R_{c2} change equally, while k and ΔR_c are fixed.

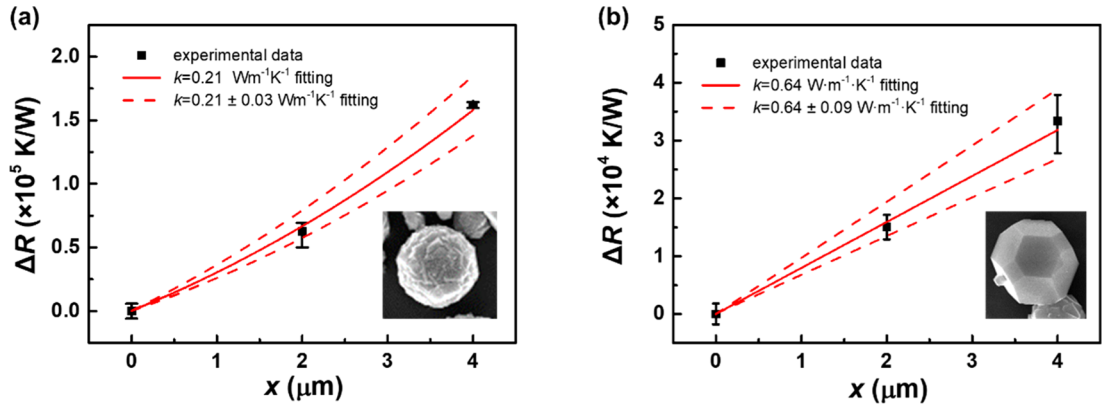

Figure 5. Dependence of the measured thermal resistance difference on the laser spot location for ZIF-8. Black squares are the experimental data, and red lines are the fitting curves. (a) Polycrystalline particle; (b) single-crystal sample. Insets show the typical morphology of the tested samples.

sample was solved numerically (Figure 4). The diameter of the laser spot is 0.57 μm according to $d = 2\lambda/(\pi \times \mathrm{NA})$. NA represents the numerical aperture of the objective lens (×40). The local temperatures of the sphere particle and RTDs denoted by T_s and T_b were governed by the steady-state heat diffusion equation in each domain, given by

$$\Delta^2 T_s = 0 \tag{4}$$

$$\Delta^2 T_b = 0 \tag{5}$$

They were coupled through the boundary conditions of the contact region. Considering thermal contact resistances and the continuity of heat flux, the boundary conditions can be written as

$$-k_s \left.\frac{\partial T_s}{\partial \mathbf{n}}\right|_{\text{interface}} = \frac{T_s - T_b}{R_c} \tag{6}$$

$$\frac{T_s - T_b}{R_c} = -k_b \left.\frac{\partial T_b}{\partial \mathbf{n}}\right|_{\text{interface}} \tag{7}$$

https://dx.doi.org/10.1021/acsnano.0c06756
ACS Nano 2020, 14, 14100−14107

where k represents thermal conductivity, R_c is the thermal contact resistance between sample and RTDs, and subscripts of s and b denote the tested sample and the RTDs, respectively. The four ends of the two suspended RTDs were all connected to heat sinks. Thus, the boundary temperatures were taken as constant temperature, T_0 = 293.15 K. Other surfaces were treated as adiabatic boundaries except for the laser heating spot, whose net heat flux is assumed to be constant. The governing equation and the boundary conditions were solved using finite element methods. The relative tolerance is set to 10^{-5}. In practical measurement, the two thermal contact resistances are not identical. Therefore, they were set to different values. Figure 4b shows the difference between the measured thermal resistances (ΔR) as a function of laser spot locations (x) by employing different thermal conductivities (k), but identical thermal contact resistances (R_{c1} and R_{c2}). It can be found that the ΔR–x curve gets steeper as the thermal conductivity decreases. At fixed k and R_{c1}, the ΔR–x curve shifts downward when the difference between two thermal contact resistances ($\Delta R_c = R_{c1} - R_{c2}$) increases as shown in Figure 4c. Similarly, by equally increasing R_{c1} and R_{c2} (k and ΔR_c remain unchanged), the ΔR–x curve shifts downward, and the change rate of the curve is nearly unchanged (Figure 4d). It can be concluded that R_{c1} and R_{c2} will only affect the value of ΔR (the relative position of ΔR–x curve) but not the shape of the ΔR–x curve. In contrast, the shape of the ΔR–x curve is dominated by the thermal conductivity of the sample. Thus, we can derive the thermal conductivity of the tested samples by fitting the experimentally measured ΔR–x curve.

According to eqs 1–3, the dependence of thermal resistance difference ΔR on the laser spot location x can be obtained. Figure 5a and b show the ΔR–x curves of polycrystalline and single-crystal ZIF-8 particles, respectively. The temperature rise at the laser heating spot was measured to be 19–35 K. Besides, ZIF-8 possesses high thermal stability.[35] Thus, the crystal structure of the sample has not been changed during measurement. Furthermore, the thermal conductivities of MOFs are nearly temperature independent above 200 K according to previous experimental and theoretical studies.[24,36] Therefore, the laser heating will not impose any undesirable influences on the thermal conductivity measurement. The error bars reflect the uncertainty of ΔR caused by temperature sensing based on Raman scattering (ΔT_h). The temperature measurement uncertainty of the RTDs is less than 0.05 K, which is significantly lower than the uncertainty of Raman-based temperature sensing (~2 K in this measurement); thus the influence of the temperature measurement uncertainty of the RTDs on ΔR measurement uncertainty can be ignored. As depicted in Figure S3, the spherical particle possesses many grain boundaries and a rough surface, which indicates a polycrystalline structure. The single-crystal ZIF-8 has the shape of a chamfered cube as shown in Figure S4. The chamfered cube is a convex polyhedron with 32 vertices, 48 edges, and 18 faces: 12 hexagons and 6 squares, whose morphology is highly symmetric in all directions (x, y, and z) as well as rotational symmetry. Thus, it is reasonable to assume the single-crystal ZIF-8 as a sphere for simplicity in theoretical analysis.

The thermal conductivity of a polycrystalline ZIF-8 particle is derived to be 0.21 $W \cdot m^{-1} \cdot K^{-1}$ by fitting the experimental data (solid line in Figure 5a). The theoretical fitting curves of 0.18 and 0.24 $W \cdot m^{-1} \cdot K^{-1}$ are also plotted (dashed lines in Figure 5a), suggesting that the proposed Raman-RTDs method has very high measurement sensitivity. The measurement was conducted when the optimal focusing conditions of the laser were achieved. Thus, the size of the laser spot remained constant during measurement and would not affect the result of thermal conductivity. Besides, our method is applicable to different laser spot radii as long as it meets the requirement of special resolution for obtaining the relationship between ΔR and x. Certainly, the smaller laser spot size enables a more accurate measurement of ΔR–x relationship and a higher measurement sensitivity of thermal conductivity (Figure S9).

As for the ZIF-8 single crystal, the sample size is considered as its circumscribed diameter, *i.e.*, 20.9 μm. The thermal conductivity of single-crystal ZIF-8 is derived to be 0.64 $W \cdot m^{-1} \cdot K^{-1}$, which is consistent with the expected order of magnitude from molecular dynamic (MD) simulation (0.165 $W \cdot m^{-1} \cdot K^{-1}$).[37] The thermal conductivity of a ZIF-8 single crystal is also higher than that of the polycrystalline sample. It is mainly due to the extra thermal resistances resulting from the grain boundaries and defects in the ZIF-8 polycrystal.[33] Overall, the measured thermal conductivities of ZIF-8 samples are on the same order of magnitude as other types of MOFs that have been measured experimentally.[15,24,25] The thermal conductivities of MOFs are rather low as a crystal material. This feature can be interpreted considering its crystal structure. First, MOFs are nanoporous crystals with very high porosity, in which the wide spreading void phase inside the crystal can reduce the effective cross-section area of the heat conduction path. Second, MOF crystals are composed of metal nodes and organic linkers. The large mismatch between vibrational density of states (VDOS) of metal nodes (Zn) and organic linkers (N) (see Figure S10 for details) in ZIF-8 may cause interfacial phonon scattering, which suppresses phonon transport at the junction and reduces the thermal conductivity.[37]

A comparison of experimentally measured thermal conductivity of ZIF-8 in different forms is presented in Figure 6. It can be found that the thermal conductivity of compacted ZIF-8 powders measured by a homemade transient hot-wire approach[15] (0.029 $W \cdot m^{-1} \cdot K^{-1}$) is obviously lower than the result of a single particle measured in this work, which is

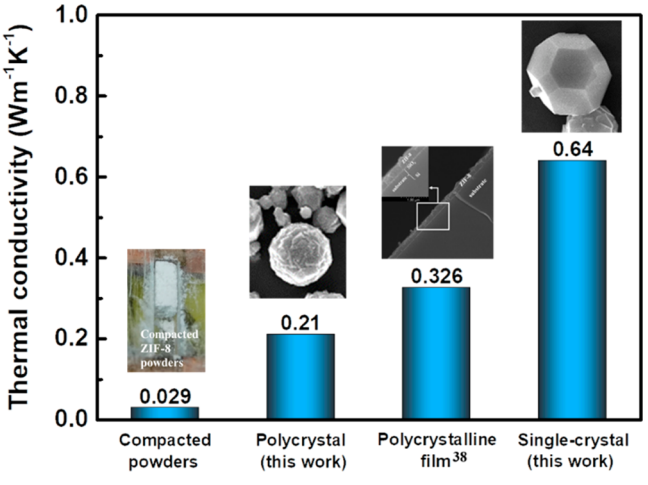

Figure 6. Comparison of ZIF-8 thermal conductivity among our measurement results and previously published results. The insets show the morphology of tested samples. The SEM image of the polycrystalline film was reproduced with permission from ref 38. Copyright 2017 American Chemical Society.

https://dx.doi.org/10.1021/acsnano.0c06756
ACS Nano 2020, 14, 14100–14107

Table 2. Comparisons of Different Thermal Conductivity Measurement Methods for MOFs

	flash method[14,19,20,40]	transient plane source method[13]	transient hot-wire method[15]	3-ω method[38]	steady-state method[24,25]	Raman-RTDs method
sample	MOF-5	MOF-5	UiO-66;UiO-67;Cu-BTC; ZIF-8	ZIF-8	MOF-5; MOF-1	ZIF-8
sample morphology	compacted powders (cylindrical pellets)	compacted powders (cylindrical pellets)	compacted powders (rectangular pellets)	polycrystalline thin film	single crystal	single crystal
sample dimension	12 mm (diameter)	50 mm (diameter)	20 × 5 × 6 mm	300 nm (thickness)	1 mm	20.9 μm
measurement uncertainty from ICTR	yes	yes	yes	yes	no	no
measurement uncertainty from TCR	yes	yes	yes	yes	yes	no

ascribed to the extensive thermal contact resistance between particles for the transient hot-wire approach. Until now, there is no measurement result of the thermal conductivity of single-crystal ZIF-8. The only experimental measurement has been conducted on a ZIF-8 polycrystalline film[38] with a thermal conductivity of 0.326 $W{\cdot}m^{-1}{\cdot}K^{-1}$, which is higher than the results of a ZIF-8 polycrystalline particle obtained by our Raman-RTDs method. One possible reason could be the different amounts/positions of grain boundaries and defects between our polycrystalline particle and the polycrystalline film. Another possible reason is that the film degraded during the thermal conductivity measurement. The degradation of the film is an endothermic process, so that the measured temperature oscillation is lower than that caused by the heat dissipation alone. As a result, the thermal conductivity of the ZIF-8 film could be overestimated according to the 3-ω method.[38,39] Comparing with the predicted value from MD simulation (0.165 $W{\cdot}m^{-1}{\cdot}K^{-1}$),[37] our experimental results are consistent in the order of magnitude.

Comparisons of different thermal conductivity measurement methods for MOFs are shown in Table 2. Until now, most measurements were conducted on compacted MOF powders by the flash method,[14,19,20,40] transient plane source method,[13] or transient hot-wire method,[15] all of which suffer from the measurement uncertainty induced by the intercrystal thermal resistance (ICTR) and the thermal contact resistance (TCR) between sample and sensor. The ICTR can be further subdivided into two components: the interparticle thermal contact resistance between two adjacent crystals and the thermal resistance of the grain boundary inside the polycrystalline particle. Therefore, the thermal conductivity of the MOF crystal itself can hardly be derived from the result of compacted powder or pellet samples. Another drawback of these methods is that the required amount of MOF sample is relatively large compared to the limited yield of MOF synthesis. The 3-ω method has been used to measure the thermal conductivity of a ZIF-8 thin film. Although the sample was an individual crystal, it is still a polycrystalline sample, and there were grain boundaries inside. Therefore, the influence of ICTR still existed. As for the steady-state method, due to the difficulty in monitoring the temperature difference and the heat flux at the sample surface, only a large-size single crystal can be successfully measured. There was no grain boundary inside the single-crystal samples compared to the polycrystalline samples measured in the 3-ω method. As a result, the steady-state method is not affected by the ICTR of the sample. However, it suffers from the measurement uncertainty induced by the TCR between sample and temperature sensor, similar to the 3-ω method. On the contrary, the thermal conductivity of single-crystal ZIF-8 was measured directly in our Raman-RTDs method without the influence of both ICTR and TCR, and the size limit of the sample is reduced to the order of 10 μm, which enables the measurement of MOF crystals with a wide range of sample sizes.

It should also be noted that there are several factors that may cause measurement errors of thermal conductivity. First, the uncertainty of the RTDs' thermal conductivities will influence the measurement of ΔR by altering the heat flux Q (eq 2). The error of thermal conductivity measurement resulting from it was analyzed to be less than ± 0.03 $W{\cdot}m^{-1}{\cdot}K^{-1}$ (see Figure S11 for details). Second, from the SEM results of tested samples, it can be observed that the polycrystalline particle has the shape of a sphere with a rough surface. The measurement error of thermal conductivity induced by the uncertainty of characterizing the particle radius was also analyzed (shown in Figure S12). When the measurement uncertainty of the sample radius is 0.5 μm, the error of the thermal conductivity is ± 0.01 $W{\cdot}m^{-1}{\cdot}K^{-1}$. Third, the error caused by taking the chamfered cubic crystal as a spherical sample was preliminarily estimated as 0.09 $W{\cdot}m^{-1}{\cdot}K^{-1}$ by comparing the results of the circumsphere model and the inscribed sphere model (Figure S13).

Our Raman-RTDs method is simple and reliable. In principle, our method is also applicable to other MOFs regardless of the morphology as long as the corresponding heat conduction model can be constructed. The only requirements for the tested samples are that the Raman spectra should be temperature-dependent and that the minimum sample radius should not be less than 7 μm to ensure a constant laser spot size at different measuring points. The temperature dependence of the Raman shift is also validated for Cu-BTC (see details in Figure S14). However, it remains a great challenge to derive the thermal conductivity for such a nonspherical sample due to the difficulty in precisely reconstructing the corresponding heat conduction model, which requires intensive exploration in future work.

CONCLUSION

In this work, we reported the Raman-RTDs method for *in situ* thermal conductivity measurement of a single-crystal MOF. In this approach, two suspended Si_3N_4/Pt RTDs were fabricated as both sample holder and temperature sensor, which ensures an accurate determination of the temperature rise and heat flux in small regions on the sample surface. The thermal conductivity of the MOF crystal and the thermal contact resistance between the MOF crystal and the RTDs were

https://dx.doi.org/10.1021/acsnano.0c06756
ACS Nano 2020, 14, 14100−14107

quantified simultaneously by our *in situ* Raman-RTDs method, which helps to eliminate the system error caused by the thermal contact resistance and gives a more accurate and reliable thermal conductivity. This work demonstrated a viable *in situ* Raman-RTDs method for obtaining the thermal conductivity of microscale MOF crystals with high accuracy, which may be extended to other families of microscale materials in the future.

METHODS

Synthesis and Characterization of ZIF-8. $Zn(NO_3)_2{\cdot}6H_2O$ (1.49 g, 5 mmol) was dissolved in methanol (100 mL). 2-Methylimidazole (0.82 g, 10 mmol) and sodium formate (1.36 g, 20 mmol) were dissolved in methanol (100 mL). The latter solution was poured into the former solution with stirring until complete mixing. Next, the solution was heated to 363 K and maintained for 24 h. Then, the white solid was isolated by centrifugation and washed with methanol (30 mL) three times. Finally, the solid was dried in air at room temperature for 5 h and then dried under vacuum at 453 K for 24 h.

Powder X-ray diffraction (PXRD) data were collected on a PANalytical X'Pert X-ray diffractometer in reflection mode using Cu Kα (λ = 1.540 598 Å) radiation. The power rating of the X-ray generator was adjusted to 40 kV and 40 mA. The 2θ ranges from 5° to 50° as a continuous scan with a step size of 0.013 13° at room temperature. The measured PXRD pattern in Figure S5 is consistent with the simulated results, indicating that the high purity and crystallinity of the prepared samples. The shape of the ZIF-8 crystal was observed by the optical microscope equipped in the micromanipulation system (Micro Support, Axis Pro SS).

Fabrication of Suspended Si_3N_4/Pt RTDs. First, a Si_3N_4 wafer was etched using the RIE technique to form two strips with a thickness of 0.2 μm. Then, a 0.1-μm-thick platinum film was deposited on an evenly patterned 5-nm-thick chromium adhesion layer by physical vapor deposition (PVD). The pattern of the platinum film was controlled by a precisely processed mask. The bottom Si_3N_4 layer provides sufficient mechanical strength and electrical insulation, while the upper platinum layer works as a temperature sensor that converts the temperature signal to electrical resistance. The fabricated Si_3N_4/Pt RTDs is shown in Figure 1c after removing the photoresist. Finally, copper wires were attached onto the contact pads with conductive silver paste for electrical measurements.

Thermal Conductivity Measurement. The schematic of the Raman-RTDs method is demonstrated in Figure 3. A ZIF-8 crystal was manipulated and placed in between the two RTDs using a micromanipulation system (Micro Support, Axis Pro SS). Then, they were put on a temperature-controlled stage (Linkam, THMS350EV-4) with a 0.1 K temperature resolution, and the measurement was done in a vacuum of 10^{-4} Pa to eliminate convective heat transfer. The tested crystal was heated by a continuous wave laser with a wavelength of 532 nm, which was focused by an Olympus 40× objective lens whose numerical aperture is 0.60. The Raman spectra of the ZIF-8 crystal were measured by a Horiba T64000 Raman spectroscope. Electrical resistances of two Pt/Si_3N_4 RTDs were measured by digital multimeters (Keitheley 2002) simultaneously. The thermal resistance of the ZIF-8 crystal was then obtained by dividing the temperature difference between the laser spot and the RTD contact point by the heat flux flowing through the corresponding RTDs. Thermal conductivity of ZIF-8 was extracted from the dependence of the measured thermal resistance of the ZIF-8 crystal on the laser spot location.

ASSOCIATED CONTENT

Supporting Information

The Supporting Information is available free of charge at https://pubs.acs.org/doi/10.1021/acsnano.0c06756.

Characteristics of the ZIF-8 crystal; thermal conductivity measurement of Si_3N_4/Pt RTDs and its influence on thermal resistance difference measurement uncertainty; calibration of the temperature dependence of Raman shifts of the tested ZIF-8 sample; measurement sensitivity analysis of the Raman-RTDs method; lattice dynamics analysis of the ZIF-8 crystal; measurement error analysis of the Raman-RTDs method; calibration of the temperature dependence of Raman shifts of the Cu-BTC crystal (PDF)

AUTHOR INFORMATION

Corresponding Authors

Xing Zhang − *Key Laboratory for Thermal Science and Power Engineering of Ministry of Education, Department of Engineering Mechanics, Tsinghua University, Beijing 100084, China;* orcid.org/0000-0001-7294-9598; Email: x-zhang@mail.tsinghua.edu.cn

Song Li − *State Key Laboratory of Coal Combustion, School of Energy and Power Engineering, Huazhong University of Science and Technology, Wuhan 430074, China*; Email: songli@hust.edu.cn

Authors

Jun Huang − *Key Laboratory for Thermal Science and Power Engineering of Ministry of Education, Department of Engineering Mechanics, Tsinghua University, Beijing 100084, China;* orcid.org/0000-0001-9190-9233

Aoran Fan − *Key Laboratory for Thermal Science and Power Engineering of Ministry of Education, Department of Engineering Mechanics, Tsinghua University, Beijing 100084, China*

Xiaoxiao Xia − *State Key Laboratory of Coal Combustion, School of Energy and Power Engineering, Huazhong University of Science and Technology, Wuhan 430074, China;* orcid.org/0000-0001-9001-3662

Complete contact information is available at: https://pubs.acs.org/10.1021/acsnano.0c06756

Notes

The authors declare no competing financial interest.

ACKNOWLEDGMENTS

This work was supported by the National Natural Science Foundation of China (Grant Nos. 51827807, 51636002), Science Fund for Creative Research Groups (No. 51621062), Hubei Provincial Nature Science Foundation (No. 2019CFB456), and double first-class research funding of China-EU Institute for Clean and Renewable Energy (No. ICARE-RP-2018-HYDRO-001).

REFERENCES

(1) Rosi, N. L.; Eckert, J.; Eddaoudi, M.; Vodak, D. T.; Kim, J.; Keeffe, M.; Yaghi, O. M. Hydrogen Storage in Microporous Metal-Organic Frameworks. *Science* **2003**, *300*, 1127−1129.

(2) Ahmed, A.; Seth, S.; Purewal, J.; Wong-Foy, A. G.; Veenstra, M.; Matzger, A. J.; Siegel, D. J. Exceptional Hydrogen Storage Achieved by Screening Nearly Half a Million Metal-Organic Frameworks. *Nat. Commun.* **2019**, *10*, 1−9.

(3) Meek, S. T.; Greathouse, J. A.; Allendorf, M. D. Metal-Organic Frameworks: A Rapidly Growing Class of Versatile Nanoporous Materials. *Adv. Mater.* **2011**, *23*, 249−267.

(4) Li, Q.; Liu, Q.; Zhao, J.; Hua, Y.; Sun, J.; Duan, J.; Jin, W. High Efficient Water/Ethanol Separation by a Mixed Matrix Membrane Incorporating MOF Filler with High Water Adsorption Capacity. *J. Membr. Sci.* **2017**, *544*, 68−78.
(5) Henninger, S. K.; Jeremias, F.; Kummer, H.; Janiak, C. MOFs for Use in Adsorption Heat Pump Processes. *Eur. J. Inorg. Chem.* **2012**, *2012*, 2625−2634.
(6) AL-Dadah, R.; Mahmoud, S.; Elsayed, E.; Youssef, P.; Al-Mousawi, F. Metal-Organic Framework Materials for Adsorption Heat Pumps. *Energy* **2020**, *190*, 116356.
(7) Kim, H.; Yang, S.; Rao, S. R.; Narayanan, S.; Kapustin, E. A.; Furukawa, H.; Umans, A. S.; Yaghi, O. M.; Wang, E. N. Water Harvesting from Air with Metal-Organic Frameworks Powered by Natural Sunlight. *Science* **2017**, *356*, 430−434.
(8) Kalmutzki, M. J.; Diercks, C. S.; Yaghi, O. M. Metal−Organic Frameworks for Water Harvesting from Air. *Adv. Mater.* **2018**, *30*, 1704304.
(9) Li, B.; Wen, H. M.; Zhou, W.; Chen, B. Porous Metal-Organic Frameworks for Gas Storage and Separation: What, How, and Why? *J. Phys. Chem. Lett.* **2014**, *5*, 3468−3479.
(10) Furukawa, H.; Ko, N.; Go, Y. B.; Aratani, N.; Choi, S. B.; Choi, E.; Yazaydin, A. Ö.; Snurr, R. Q.; O'Keeffe, M.; Kim, J.; Yaghi, O. M. Ultrahigh Porosity in Metal-Organic Frameworks. *Science* **2010**, *329*, 424−428.
(11) Wang, H.; Qu, Z. G.; Zhang, W.; Yu, Q. N.; He, Y. L. Experimental and Numerical Study of CO2 Adsorption on Copper Benzene-1,3,5-Tricarboxylate (Cu-BTC) Metal Organic Framework. *Int. J. Heat Mass Transfer* **2016**, *92*, 859−863.
(12) Ming, Y.; Purewal, J.; Liu, D.; Sudik, A.; Xu, C.; Yang, J.; Veenstra, M.; Rhodes, K.; Soltis, R.; Warner, J.; Gaab, M.; Müller, U.; Siegel, D. J. Thermophysical Properties of MOF-5 Powders. *Microporous Mesoporous Mater.* **2014**, *185*, 235−244.
(13) Semelsberger, T. A.; Veenstra, M.; Dixon, C. Room Temperature Thermal Conductivity Measurements of Neat MOF-5 Compacts with High Pressure Hydrogen and Helium. *Int. J. Hydrogen Energy* **2016**, *41*, 4690−4702.
(14) Purewal, J. J.; Liu, D.; Yang, J.; Sudik, A.; Siegel, D. J.; Maurer, S.; Müller, U. Increased Volumetric Hydrogen Uptake of MOF-5 by Powder Densification. *Int. J. Hydrogen Energy* **2012**, *37*, 2723−2727.
(15) Huang, J.; Xia, X.; Hu, X.; Li, S.; Liu, K. A General Method for Measuring the Thermal Conductivity of MOF Crystals. *Int. J. Heat Mass Transfer* **2019**, *138*, 11−16.
(16) Sun, L.; Liao, B.; Sheberla, D.; Kraemer, D.; Zhou, J.; Stach, E. A.; Zakharov, D.; Stavila, V.; Talin, A. A.; Ge, Y.; Allendorf, M. D.; Chen, G.; Léonard, F.; Dincă, M. A Microporous and Naturally Nanostructured Thermoelectric Metal-Organic Framework with Ultralow Thermal Conductivity. *Joule.* **2017**, *1*, 168−177.
(17) Sørensen, S. S.; Østergaard, M. B.; Stepniewska, M.; Johra, H.; Yue, Y.; Smedskjaer, M. M. Metal-Organic Framework Glasses Possess Higher Thermal Conductivity than Their Crystalline Counterparts. *ACS Appl. Mater. Interfaces* **2020**, *12*, 18893−18903.
(18) Qu, Z.-G.; Wang, H.; Zhang, W. Highly Efficient Adsorbent Design Using a Cu-BTC/CuO/Carbon Fiber Paper Composite for High CH4/N2 Selectivity. *RSC Adv.* **2017**, *7*, 14206−14218.
(19) Liu, D.; Purewal, J. J.; Yang, J.; Sudik, A.; Maurer, S.; Mueller, U.; Ni, J.; Siegel, D. J. MOF-5 Composites Exhibiting Improved Thermal Conductivity. *Int. J. Hydrogen Energy* **2012**, *37*, 6109−6117.
(20) Ming, Y.; Chi, H.; Blaser, R.; Xu, C.; Yang, J.; Veenstra, M.; Gaab, M.; Müller, U.; Uher, C.; Siegel, D. J. Anisotropic Thermal Transport in MOF-5 Composites. *Int. J. Heat Mass Transfer* **2015**, *82*, 250−258.
(21) Prasher, R. S.; Hu, X. J.; Chalopin, Y.; Mingo, N.; Lofgreen, K.; Volz, S.; Cleri, F.; Keblinski, P. Turning Carbon Nanotubes from Exceptional Heat Conductors into Insulators. *Phys. Rev. Lett.* **2009**, *102*, 105901.
(22) Wan, P.; Gao, L.; Wang, J. Approaching Ultra-Low Thermal Conductivity in β-SiC Nanoparticle Packed Beds through Multiple Heat Blocking Mechanisms. *Scr. Mater.* **2017**, *128*, 1−5.
(23) Kovalev, O. B.; Gusarov, A. V. Modeling of Granular Packed Beds, Their Statistical Analyses and Evaluation of Effective Thermal Conductivity. *Int. J. Therm. Sci.* **2017**, *114*, 327−341.
(24) Huang, B. L.; Ni, Z.; Millward, A.; McGaughey, A. J. H.; Uher, C.; Kaviany, M.; Yaghi, O. Thermal Conductivity of a Metal-Organic Framework (MOF-5): Part II. Measurement. *Int. J. Heat Mass Transfer* **2007**, *50*, 405−411.
(25) Gunatilleke, W. D. C. B.; Wei, K.; Niu, Z.; Wojtas, L.; Nolas, G.; Ma, S. Thermal Conductivity of a Perovskite-Type Metal−Organic Framework Crystal. *Dalt. Trans.* **2017**, *46*, 13342−13344.
(26) Chien, H. C.; Peng, W. T.; Chiu, T. H.; Wu, P. H.; Liu, Y. J.; Tu, C. W.; Wang, C. L.; Lu, M. C. Heat Transfer of Semicrystalline Nylon Nanofibers. *ACS Nano* **2020**, *14*, 2939−2946.
(27) Shi, L.; Li, D.; Yu, C.; Jang, W.; Kim, D.; Yao, Z.; Kim, P.; Majumdar, A. Measuring Thermal and Thermoelectric Properties of One-Dimensional Nanostructures Using a Microfabricated Device. *J. Heat Transfer* **2003**, *125*, 881−888.
(28) Fujii, M.; Zhang, X.; Xie, H.; Ago, H.; Takahashi, K.; Ikuta, T.; Abe, H.; Shimizu, T. Measuring the Thermal Conductivity of a Single Carbon Nanotube. *Phys. Rev. Lett.* **2005**, *95*, 65502.
(29) Cahill, D. G. Thermal Conductivity Measurement from 30 to 750 K: The 3ω Method. *Rev. Sci. Instrum.* **1990**, *61*, 802−808.
(30) Paddock, C. A.; Eesley, G. L. Transient Thermoreflectance from Thin Metal Films. *J. Appl. Phys.* **1986**, *60*, 285−290.
(31) Fan, A.; Hu, Y.; Ma, W.; Wang, H.; Zhang, X. Dual-Wavelength Laser Flash Raman Spectroscopy Method for *In-Situ* Measurements of the Thermal Diffusivity: Principle and Experimental Verification. *J. Therm. Sci.* **2019**, *28*, 159−168.
(32) Hu, Y.; Fan, A.; Liu, J.; Wang, H.; Ma, W.; Zhang, X. A Dual-Wavelength Flash Raman Method for Simultaneously Measuring Thermal Diffusivity and Line Thermal Contact Resistance of an Individual Supported Nanowire. *Thermochim. Acta* **2020**, *683*, 178473.
(33) Zhang, K.; Lively, R. P.; Zhang, C.; Koros, W. J.; Chance, R. R. Investigating the Intrinsic Ethanol/Water Separation Capability of ZIF-8: An Adsorption and Diffusion Study. *J. Phys. Chem. C* **2013**, *117*, 7214−7225.
(34) de Lange, M. F.; Verouden, K. J. F. M.; Vlugt, T. J. H.; Gascon, J.; Kapteijn, F. Adsorption-Driven Heat Pumps: The Potential of Metal−Organic Frameworks. *Chem. Rev.* **2015**, *115*, 12205−12250.
(35) Park, K. S.; Ni, Z.; Côté, A. P.; Choi, J. Y.; Huang, R.; Uribe-Romo, F. J.; Chae, H. K.; O'Keeffe, M.; Yaghi, O. M. Exceptional Chemical and Thermal Stability of Zeolitic Imidazolate Frameworks. *Proc. Natl. Acad. Sci. U. S. A.* **2006**, *103*, 10186−10191.
(36) Huang, B. L.; McGaughey, A. J. H.; Kaviany, M. Thermal Conductivity of Metal-Organic Framework 5 (MOF-5): Part I. Molecular Dynamics Simulations. *Int. J. Int. J. Heat Mass Transfer* **2007**, *50*, 393−404.
(37) Zhang, X.; Jiang, J. Thermal Conductivity of Zeolitic Imidazolate Framework-8: A Molecular Simulation Study. *J. Phys. Chem. C* **2013**, *117*, 18441−18447.
(38) Cui, B.; Audu, C. O.; Liao, Y.; Nguyen, S. T.; Farha, O. K.; Hupp, J. T.; Grayson, M. Thermal Conductivity of ZIF-8 Thin-Film under Ambient Gas Pressure. *ACS Appl. Mater. Interfaces* **2017**, *9*, 28139−28143.
(39) Cahill, D. G. Thermal Conductivity Measurement from 30 to 750 K: The 3ω Method. *Rev. Sci. Instrum.* **1990**, *61*, 802−808.
(40) Ming, Y.; Purewal, J.; Liu, D.; Sudik, A.; Xu, C.; Yang, J.; Veenstra, M.; Rhodes, K.; Soltis, R.; Warner, J.; Gaab, M.; Müller, U.; Siegel, D. J. Thermophysical Properties of MOF-5 Powders. *Microporous Mesoporous Mater.* **2014**, *185*, 235−244.

https://dx.doi.org/10.1021/acsnano.0c06756
ACS Nano 2020, 14, 14100−14107